J. Fluid Mech. (1997), *vol.* 338, *pp.* 173–201

Printed in the United Kingdom © 1997 Cambridge University Press

Drop fall-off from pendent rivulets

By ALEXANDRA INDEIKINA, IGOR VERETENNIKOV AND HSUEH-CHIA CHANG

Department of Chemical Engineering,
University of Notre Dame, Notre Dame, IN 46556, USA

(Received 6 July 1996 and in revised form 11 November 1996)

Drops fall off a viscous pendent rivulet on the underside of a plane when the inclination angle θ, measured with respect to the horizontal, is below a critical value θ_c. We estimate this θ_c by studying the existence of finite-amplitude drop solutions to a long-wave lubrication equation. Through a partial matched asymptotic analysis, we establish that fall-off occurs by two distinct mechanisms. For $\theta > \varphi$, where φ is the static contact angle, a jet mechanism results when a mean-flow steepening effect cannot provide sufficient axial curvature to counter gravity. This fall-off mechanism occurs if the rivulet width B, which is normalized with respect to the capillary length $H = (\sigma/\rho g \cos\theta)^{1/2}$, exceeds a critical value defined by $\beta = -\cos B > 1/4$. For $\theta < \varphi$, the normal azimuthal curvature is the dominant force against fall-off and the azimuthal capillary force. The corresponding critical condition is found to be $1.5\beta^{1/6} > \tan\theta/\tan\varphi$. Both criteria are in good agreement with our experimental data.

1. Introduction

Many hydrodynamic instabilities are known to yield localized structures in addition to or instead of the classical global sinuous waves with a narrow band of Fourier modes. The latter wave field consists of waves much shorter and smaller than the characteristic depth of the system and is commonly known as a short-wave instability. Near criticality, the dynamics of these small and short waves is well-described by the traditional weakly nonlinear amplitude equations, like the coupled complex Ginzburg–Landau (CGL) equation (Manneville 1990). The width and amplitude of the localized structures, on the other hand, are much larger than the characteristic system depth. They are hence referred to as a long-wave instability (Van Hook *et al.* 1995) even though their structures are not at all wave-like. A rational theory for the existence and dynamics of these localized structures is an active area of research in hydrodynamics and we examine a specific example here.

There is growing evidence that many classical hydrodynamic instabilities are dominated by the localized structures. Localized patterns, in addition to short waves, are observed in Couette flow (Cherhabili & Ehrenstein 1995), Faraday instability (Kudrolli & Gollub, 1996) and in shear boundary layer instabilities (Kachanov 1994) where the waves at inception are clearly of the short variety but they seem to synchronize to form the localized structures. However, localized structures are most prevalent in interfacial instabilities where even the small-amplitude waves at inception are long and they 'focus' into the localized structures. Falling-film wave dynamics is dominated by localized 'pulses' (Pumir, Manneville & Pomeau 1983; Chang 1994)

https://doi.org/10.1017/S0022112096004879 Published online by Cambridge University Press

and drops (Quere 1990). Dry spots that form on heated films (Joo, Davis & Bankoff 1991*a*) and films undergoing Marangoni convection (Van Hook *et al.* 1995), slugs that grow from stratified gas-liquid flow (McCready & Chang 1996), bubble formation in capillaries (Hammond 1983; Aul & Olbricht 1990), beading from narrow rivulets with mobile contact lines (Young & Davis 1987) and from liquid cylinders (Russo & Steen 1989) are all examples of localized interfacial structures.

Once formed, these localized structures interact with each other and with the short waves. The interaction often involves irreversible coalescence of two structures or absorption of short waves so the wave texture actually coarsens (Chang, Demekhin & Kalaidin 1995). However, an even more intriguing dynamics of the localized structures is that they can grow very rapidly in amplitude while retaining their width. This phenomenon is observed in dry spot formation (Van Hook *et al.* 1995), drop ejection from localized structures in the Faraday instability, drop formation during wire coating (Quere 1990) and, in general, any drop ejection or fall-off mechanisms. The growth is so rapid and the structure so localized in space that, if the model equation is incapable of such resolution, the phenomenon is described by a finite-time 'blow-up' solution to the equation. Since blow-up solutions can now be detected numerically and sometimes estimated analytically, there is considerable interest in using the blow-up behaviour to predict the onset of drop formation, ejection or fall off. Joo, Davis & Bankoff (1991*b*) and Rosenau, Oron & Hyman (1992) numerically explored a large class of lubrication equations and found blow-up behaviour in many of them. These Benney-type equations assume that the structure amplitude is much smaller than its width. Any structure with an aspect ratio of unit order would escape the description of the lubrication equation and their formation would correspond to a blow-up behaviour.

In the numerical studies of Joo *et al.* (1991*b*) and Rosenau *et al.* (1992), it was found that blow-up can be suppressed when a mean-flow term is added to the lubrication equation. This is consistent with the numerical results of Van Hook *et al.* (1995) and Joo *et al.* (1991*a*) for dry spot formation on a heated film. On a horizontal film, a blow-up solution, which resembles the experimentally observed dry spots, is always detected from the lubrication equation. However, when the plane is tilted, such solutions are not observed and dry spots do not appear in the experiments either.

However, numerical search for blow-up behaviour is extremely tedious and an analytical estimate of its existence would be most convenient. Oron & Rosenau (1989) and Chen & Steen (1996) examined the existence of saturated small-amplitude solutions to the lubrication equations and use that as a sufficient condition for blow-up not to occur – their non-existence is a necessary condition for blow-up. Their saturated solutions are assumed to be either spatially periodic or confined to a finite box to simplify the bifurcation analysis. While this is a valid description to study whether liquid drains out of a finite slot due to Rayleigh–Taylor instability, it is generally not accurate for the evolution of localized structures in an extended domain. There, the existence of saturated periodic waves does not preclude the occurrence of blow-up. This is clearly seen in Van Hook *et al.*'s (1995) numerical solution of a particular lubrication equation where both solutions are observed. (Both structures are also observed in their experiments.)

In a recent study, Kalliadasis & Chang (1994) proposed another theoretical estimate of blow-up. They suggested that the localized blow-up behaviour is related to saturated localized traveling waves – solitary waves. These resemble the blow-up solution in shape but instead of growing, they translate at a constant speed. When the solitary waves exist and are stable, they are assumed to be the attractors to

https://doi.org/10.1017/S0022112096004879 Published online by Cambridge University Press

all initial conditions and blow-up behaviour seems to be absent. It is only when they cease to exist that blow-up ensues. The non-existence of such solitary wave solutions to the lubrication equation then offers a good estimate of the onset of blow-up behaviour. Moreover, the solitary wave solution branch to the long-wave lubrication equation typically ceases to exist when the crest amplitude approaches infinity. While this limiting member of the branch obviously violates the long-wave approximation, it introduces a solitary wave structure with widely different length scales such that the structure and location of the limiting member can be obtained via matched asymptotic analysis. Simple criteria for the existence of solitary waves and estimates for blow-up behaviour can then be readily obtained.

This approach was successfully applied to explain Quere's data on the formation of large capillary drops, which violate the scalings of the lubrication equation, on a vertically coated wire. We found by matched asymptotic analysis that the localized solitary wave solution ceases to exist when the substrate thickness beneath it exceeds a critical value. The physical mechanism is again due to mean flow, as we shall detail subsequently. In our numerical simulation and those by Kerchman & Frenkel (1994) with a lubrication equation, the flat film (annular film around the wire) evolves into a series of solitary waves which interact and coalescence irreversibly to form larger solitary waves. Due to mass conservation, the local substrate layer thickens as the solitary wave density decreases and the critical value where no solitary wave solution exists is reached eventually. At this instant, blow-up behaviour is observed. This blow-up represents the physical formation of large capillary drops on the wire which are beyond the description of the lubrication equation. Our analytical criterion is found to be in excellent quantitative agreement with both the numerical simulations for blow-up and the physical measurements for drop formations.

In this paper, we apply the same technique to determine whether drops will fall off a pendent rivulet on the underside of a tilted plane. Unlike overlying rivulets on the top side (Weiland & Davis 1981; Young & Davis 1987), transverse surface tension forces of the meniscus actually have a stabilizing effect in countering the destablizing effect of gravity. Rothrock (1968) carried out a linear stability analysis based on a lubrication approximation and obtained the onset conditions for waves on a pendent rivulet as well as their speeds and wavelengths. These are confirmed by his experimental measurements. He also noted that these initial disturbances evolve quickly into localized solitary waves (drops) which can remain on the rivulet indefinitely or grow into much larger drops and fall off the rivulet. We shall study this demarcation carefully in our experiment and show that there is a critical inclination angle θ_c with respect to the horizontal when the fall-off begins. We shall show from a lubrication analysis that mean flow can again produce a saturated drop solution analogous to the solitary wave solution for θ larger than θ_c. It is when this and another stabilizing effect cannot counter the pull of gravity at smaller θ that the saturated solitary wave solution ceases to exist and a large drop quickly forms and falls off. As represented by the two-dimensional lubrication equation, such limiting members of the drop family have a front face with either an infinite slope (the equivalent of an infinite-amplitude solitary wave in Kalliadasis & Chang 1994) or a negative curvature. For conditions beyond the existence of these limiting drop solutions, the time evolution of the three-dimensional lubrication equation presumably leads to blow-up or singularity formation. However, the complexity of the present transient problem prevents a numerical confirmation of these behaviours similar to those carried out by Kalliadasis & Chang (1994) and Kerchman & Frenkel (1994) for drops on fibre. The additional dimension of a three-dimensional rivulet also renders

https://doi.org/10.1017/S0022112096004879 Published online by Cambridge University Press

the matched asymptotic construction of the limiting solitary drop solution difficult and only estimates of its existence are offered. Nevertheless, these estimates are in good agreement with our experimental data for fall-off and they represent the first application of this approach to realistic three-dimensional drop fall-offs.

It is important to note that while the drops are held by surface tension against the pull of gravity, the effect of surface tension is entirely determined by the shape of the drop. The shape, in turn, is governed by the rivulets in front and behind the drop due to a quasi-balance of forces. When viscous flow effects are just as dominant as capillary and gravitational forces in the rivulets, the ability of the drop to remain on the rivulet is very much dependent on the mean flow. For this reason, our fall-off mechanisms are distinct from instability of purely static pendent drops.

The physical mechanism behind how mean flow arrests localized growth deserves more study. Consider a thin lubricating film draining by gravity on either side of a plane inclined at an angle θ with respect to the horizontal. The flow rate q per cross-stream span width is determined by the balance between the tangential gravitational pull $g\sin\theta$ and kinematic viscosity v, $q = g\sin\theta h^3/3v$, where viscosity stipulates that the velocity profile is parabolic below the local interfacial height h. This scaling for gravity-driven flow of a viscous fluid provides a unique interfacial kinematic wave speed in the streamwise direction. The kinematic condition from mass conservation, $\partial h/\partial t = -\partial q/\partial x$, stipulates that the local wave speed, which is distinct from the fluid velocity, is $3g\sin\theta h^2/3v$ or three times the average velocity q/h. This is consistent with the classical result on the phase speed of small-amplitude waves on a nearly flat falling film on the top side of an inclined plane (Benjamin 1957; Yih 1963). However, it also has significant implications for the evolution of localized interfacial structures in the presence of gravity. That the wave speed is higher at a larger interfacial height implies that any localized positive disturbance will steepen at the front and become smoother at the back. Without surface tension, the nonlinear hyperbolic equation from the kinematic equation actually predicts the formation of an infinite-slope front in finite time. With surface tension, the above gravity–viscous steepening will stop at a finite slope due to the smoothing effect of capillarity which counters the formation of sharp interfacial fronts. The resulting asymmetric localized structure with a steep front, frequently preceded by some small capillary ripples, and a smooth back is found in many gravity-driven, thin-film flows where surface tension effect is important. Solitary pulses on a planar falling film (Chang 1994), drops in fibre coating (Quere 1990), fronts and fingers in a thin gravity current (Huppert 1982), drops on a rivulet, etc. all possess this unique steep-front structure. While this gravity steepening mechanism increases the interfacial slope at the front, it does not increase the amplitude of the initial disturbance. Quite the contrary, it is responsible for a unique strongly nonlinear stabilizing mechanism that reduces fluid drainage into the wave crest. The steepened front increases the axial interfacial curvature and hence induces a higher capillary pressure within the liquid immediately beneath the crest. This higher pressure reduces the flow into the crest and counters any destabilizing mechanism that magnifies the crest amplitude. On a falling film on top of an inclined plane, the growth in the wave crest stops and 'saturated' solitary pulses are formed when this effect balances the inertia-driven destabilizing mechanism. In fibre coating, it counters the Rayleigh azimuthal instability to specify the dimension of the drops (Kalliadasis & Chang 1994).

For the pendent rivulet, drainage into the drop is countered not only by the mean-flow-enhanced axial curvature but also by the azimuthal curvature. As a result, the saturated localized structure is actually a solitary drop with a surface-tension-

https://doi.org/10.1017/S0022112096004879 Published online by Cambridge University Press

rounded cross-section and a mean-flow-steepened front face. Since there are two restoring forces, the solution ceases to exist when either one cannot overcome the gravitational pull at its respective station. There will hence be two fall-off mechanisms: one corresponding to the failure of the axial curvature and one to the failure of the azimuthal curvature.

In §2, we detail our experimental measurement of the fall-off condition θ_c and demonstrate evidence of the two distinct fall-off mechanisms. In §3, we derive the lubrication equation from which we shall study the existence of saturated small-amplitude drop solutions. This is done in §4 with a matched asymptotic analysis for the three-dimensional solitary drop. Matching is only possible when two criteria, corresponding to the two fall-off mechanisms, are satisfied. These criteria are favourably compared to our experimental data in §5 where a summary and some discussion are also offered.

2. Experiments

Our experimental set-up is shown in figure 1. A glycerin–water solution is used for most of our experiments. Due to the large difference (two orders of magnitude) in the viscosity of glycerin and water, the solution provides a large range of viscosity (1 to 3 $cm^2\ s^{-1}$) simply by changing its composition via absorption of air moisture during our experiment. By carefully monitoring the viscosity, we can actually obtain the pertinent data for a wide range of physical properties without changing the fluid. The static contact angle of the glycerin–water solution is difficult to monitor continuously. Fortunately, its surface tension and wetting properties are insensitive to water composition and hence remain constant even as the viscosity changes. The solution is pumped from the lower tank 2 by a peristaltic pump 3 to upper tank 4. It overflows tank 4 on one side and a flat film is formed immediately on this vertical wall of tank 4. This film then flows around a cylinder 5 and onto the bottom of the inclined plane 1. All the above parts, including the inclined plane, are made of Plexiglas. Inclined plane 1 (width 15 cm and length 54 cm) can be tilted at any inclination angle θ with respect to the horizontal in the range of 5° and 85°. It is mounted flush against the feeding cyclinder to minimize any distortion of the film.

Rothrock (1968) has observed that a flat film on the underside of a plane destabilizes rapidly to form rivulets as a result of surface tension and gravity. A few centimetres downstream from the cylinder, these two forces begin to pull the outer edges of the film towards the middle to form a wedge shape. After a few more centimetres, the film has converged into a single straight rivulet which does not change its width for the remaining length of the plane. Since the glycerin–water solution does not wet the plane perfectly and the rivulet amplitude is relatively small, the cross-section of this rivulet resembles a segment of a cosine function. We did not measure this precisely since Rothrock has already confirmed the accuracy of this static cross-section for small-amplitude pendent rivulets.

While overlying rivulets generally suffer from a Rayleigh pinching instability and an inertial meandering instability (Weiland & Davis 1981; Young & Davis 1987) and the pendent rivulets should also be vulnerable to both, neither was observed. This was explained by Rothrock's linear instability theory of pendent rivulets which shows that for the viscous ones studied here, gravitational pull is the dominant destabilizing force. Small-amplitude sine waves generated by this instability are evident about 10 cm from the feeding cylinder (for $\theta \sim 30°$) and they rapidly focus into localized drop structures which glide down the rivulet at a large but constant speed.

https://doi.org/10.1017/S0022112096004879 Published online by Cambridge University Press

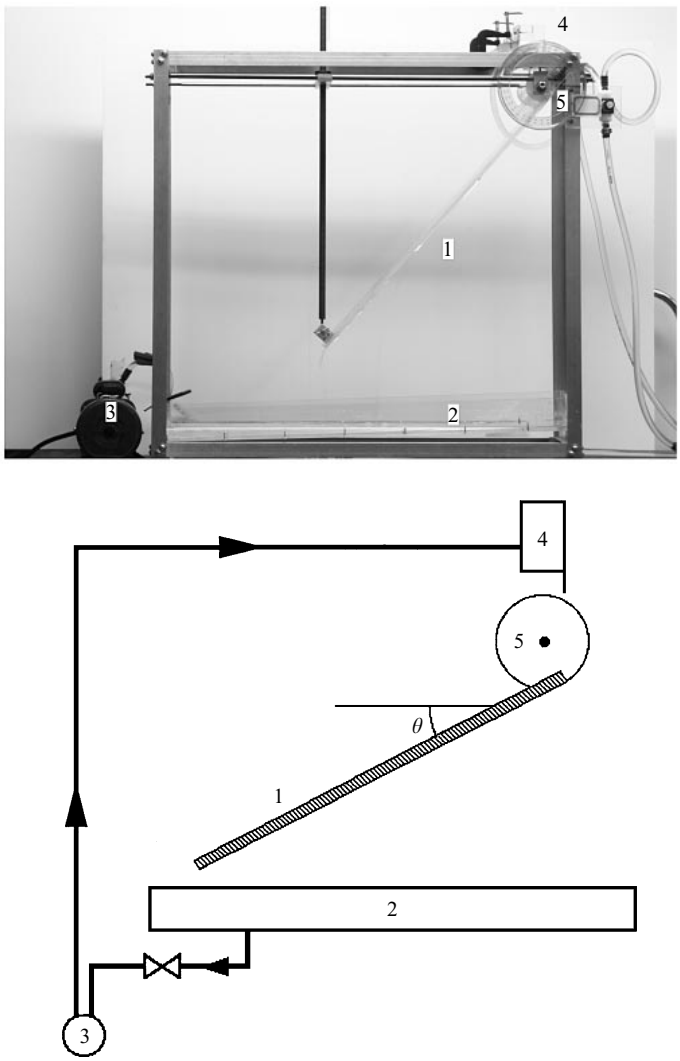


FIGURE 1. Schematic of experimental set-up. The numbered parts are described in the text.

The drops can be of various amplitudes but they are always localized in length and width. Their aspect ratio (amplitude over length) is also quite small under most conditions except when they begin to fall off. This occurs when θ falls below a critical value θ_c which depends on the flow rate q and the fluid properties. It is this θ_c that is of interest here.

Each measurement of θ_c at a given flow rate is preceded by extensive preparation. The inclined plane is wetted at a vertical position to reduce the influence of imperfections on the wettability of the Plexiglas. At this time, a flat film exists on the entire plane. After some time dewetting occurs and a single straight rivulet is formed on the dry plate. The inclination angle is then decreased slowly in steps of 1°. As the inclination angle decreases, the width of the rivulet also decreases slightly due to the effect of gravity as the contact lines move in towards the centre of the rivulet. This motion of the contact line is very slow and it is necessary to wait about 5 minutes each time the inclination angle is changed in order to equilibrate the rivulet.

https://doi.org/10.1017/S0022112096004879 Published online by Cambridge University Press

To the contrary, the width of the rivulet does not change if the inclination angle is increased, hence showing a hysteresis effect with respect to the inclination angle. Precise measurement of the width of the rivulet as a function of the inclination angle and flow rate is not carried out but it is always of the order of 1 cm. (Our theory does not provide an accurate estimate of the width. Comparison to experimental data is made through the flow rate and inclination angle, which are accurately estimated and measured.) Due to this hysteresis effect, the rivulet should be created in a similar way every time. Hence, to ensure the reproducibility of the results, the inclination angle is always varied by decreasing it.

The flow rate q and the critical angle θ_c are measured very carefully to allow comparison with our theory. Although the theory requires information on the contact-angle φ,we are unable to measure it or the cross-section shape of the rivulet accurately with our flourescence technique because the rivulet acts as a lens with very short focal distance. As a result, although the rivulet amplitude imaged from the side can be measured, the profile is beyond this technique. However, an estimate of φ can be obtained from the literature static contact angle data for water and glycerin. Because we move the plate up very slowly, the width of the rivulet decreases in a quasi-steady manner. Hence, as the rivulet shrinks, its dynamic contact angle should be close to the receding one. We expect that when the inclination angle is higher than θ_c, the dynamic contact angle then corresponds to the static value, i.e. it lies between the receding contact angle and advancing one, but is closer to the receding value. For a glycerin–water solution on Plexiglas, the static contact angle lies in the range from about 50° up to 70°, depending weakly on the composition and the temperature. Although the viscosity of our glycerin–water solution is observed to change by as much as 25% due to a 3 to 5% change in water composition, the value of φ is expected to remain constant. We shall hence choose a value between 50° and 70° to fit our data but will use the same value for all conditions. This is the only fitting parameter in our theory but it is confined to a narrow range.

At any fixed flow rate, the inclination angle is decreased in the above manner until fall-off occurs. The inclination angle is measured by means of a protractor mounted on the axis of rotation of the cylinder and is accurate to within $\pm 0.5°$. Actually, the major error in the determination of θ_c is due to ambiguity in our observation of when the first fall-off occurs. At onset, the fall-off behaviour is very localized and is intermittent in time. It hence requires a significant amount of time to ensure that fall-off does occur for some drops. However, for only 1° or 2° below θ_c all drops fall-off in a continuous manner. We hence expect θ_c to be accurate to within 3°.

The flow rate and viscosity were measured immediately after each θ_c measurement. The flow rate is determined by measuring the filling time of a cylinder of known volume and is accurate to 5%. The viscosity was measured by means of an EZ-cup viscosimeter and is accurate to 10%. During the course of our experiment the viscosity can change by as much as 25% due to water absorption. Because of the extreme sensitivity of viscosity to water content, a 3% change in water composition can be responsible for this variation. Consequently, our data actually span a large variation in the fluid viscosity and hence represent widely different fluid properties – a fortuitous consequence of the hydrophobic tendencies of glycerin.

Fluorescein sodium salt is added to the solution after the critical angle measurements to facilitate more detailed imaging of the drops and the fall-off dynamics. A black lamp is placed above the system to induce flourescence in the dye. Since the flourescence intensity is proportional to the amount of dye which is, in turn,

https://doi.org/10.1017/S0022112096004879 Published online by Cambridge University Press

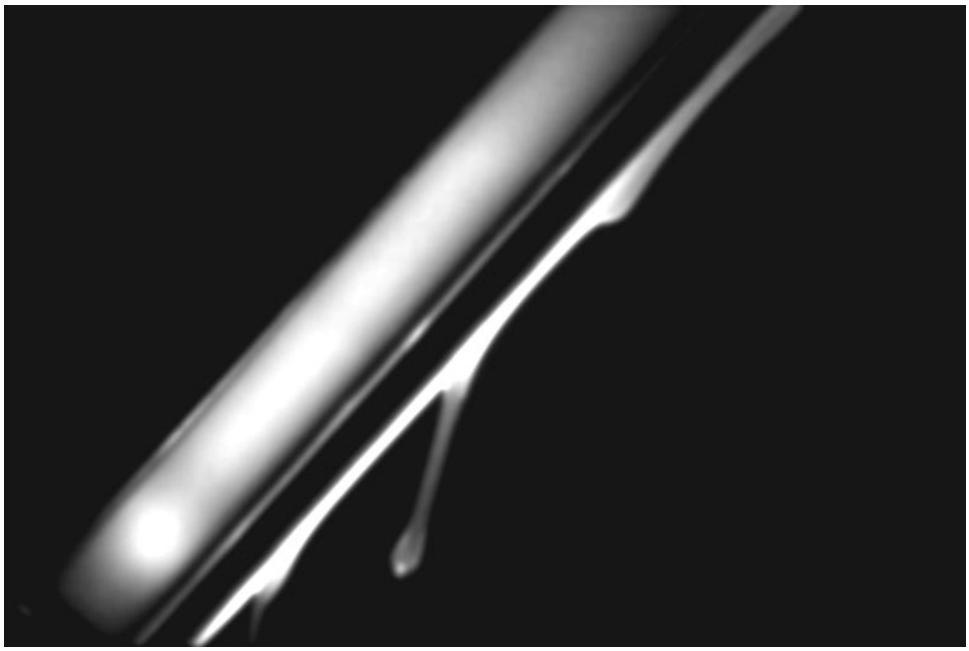


FIGURE 2. Fall-off by the jet mechanism at high flow rates. A steepened hump is observed behind the jet. (Glycerin–water solution, $\theta = 48°, \nu = 2.02$ cm^2 s^{-1} and $q = 4.7$ cm^3 s^{-1}.) The critical θ_c is 51° for this flow rate.

proportional to the film thickness, we are able to capture the interfacial shapes with a high-resolution Kodak MegaPlus 1.6 digital video camera.

The fall-off occurs by several mechanisms. At high flow rates ($q > 4.5$ cm^3 s^{-1} for the glycerin–water solution), the steepened drops are barely visible and move at a very high speed. Fall-off occurs at a small angle off vertical (large θ) and the liquid leaves the rivulet as a distinct jet as seen in figure 2. A very long steepened drop, with a small amplitude relative to the straight rivulet height and a gentle back slope, is also seen behind the jet. We call this high-flow-rate fall-off mechanism at large θ the jet mechanism. The profile of the long drop clearly takes on the linear shape of a gravity-steepened front which is the mechanism that prevents drops from evolving into jets under subcritical conditions below θ_c.

At intermediate flow rates ($0.5 < q < 4.5$ cm^3 s^{-1}), the rivulets are thinner and the drops are more pronounced compared to the rivulet and move much slower in a steady manner. The near-critical snapshot of figure 3 corresponds to this condition. As θ decreases toward θ_c, the drops clearly increase their amplitude, whose value relative to the rivulet dimension is much larger than the drops in figure 2, and steepen their front which is smoother than for the high-flow-rate conditions. They hence possess a more rounded structure than those in figure 2. After a few drops have fallen off a rivulet near θ_c, the local flow rate is lower than the feed flow rate due to the lost mass. Since θ_c decreases with decreasing flow rate (less gravitational pull for smaller rivulets), the drops adjacent to the ones that have fallen off can actually survive the traverse down the plane since they experience a lower flow rate. In the near-critical condition of figure 3, one can hence see both subcritical ($> \theta_c$) drops (front two) that do not fall off and supercritical ($< \theta_c$) drops (back two) that are in the fall-off process. We can hence record drops at various conditions away from θ_c by imaging

https://doi.org/10.1017/S0022112096004879 Published online by Cambridge University Press

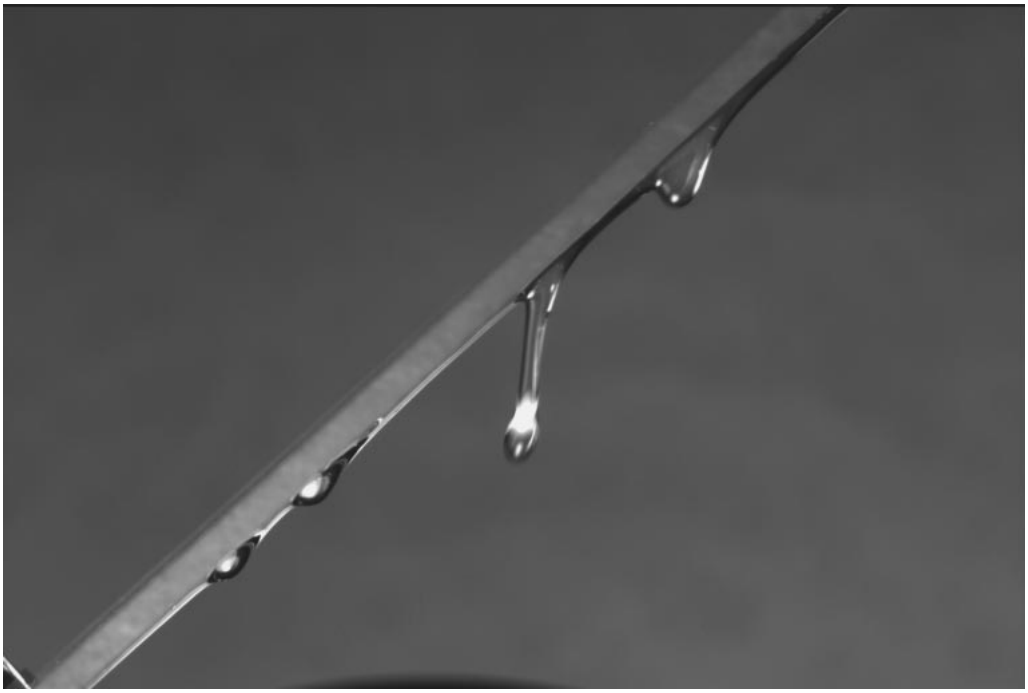


FIGURE 3. Fall-off at θ_c by the pinch-off mechanism. The last hump is barely supercritical while the first two are barely subcritical. The subcritical drops traverse the entire plane without falling off. Different drops are on different sides of criticality because, at this critical condition, a fallen drop can reduce the local flow rate to subcritical values. ($\theta = 42^\circ, v = 2.18$ cm^2 s^{-1}, $q = 2.27$ cm^3 s^{-1}.) The critical θ_c is 45° for these conditions.

the rivulet at θ close to θ_c. Snapshots of several drops prior to and during fall-off at this critical condition are shown in figure 4. While front steepening is observed, drops at this intermediate flow rate do not steepen to the extent of high-flow-rate fall-off. Instead, as seen in figures 4(*c*) and 4(*d*) and in the profiles shown in figure 5 from image processing of other snapshots, their front faces flatten and change curvature by losing their convexity such that the cross-section of the drop at that region resembles a two-dimensional pendent drop that is about to pinch off at it neck. A significant overhang at the front of the drop is seen in figure 4(*d*) and in figure 5. Beyond that, the drop beads up and pinches off from the rivulet as shown in figure 3. We refer to this intermediate-flow-rate mechanism as the pinching or pinch-off mechanism where the kinematic front-steepening effect of increasing the normal curvature is less important because of the lower flow rate. It is still necessary, however, since it conspires with the increased front face curvature due purely to capillarity to pinch off the drop prior to fall-off.

At extremely low flow rates ($q < 0.5$ cm^3 s^{-1}), the rivulet is too thin to feel a significant gravitational pull. The disturbances hence amplify very slowly and only at near-horizontal small-θ conditions such that small-amplitude waves triggered at the inlet do not have time to evolve into drops individually. Instead, they coalesce to form larger drop-like structures that fall off under supercritical conditions. This mechanism is similar to falling film dynamics on the top side of a plane (Chang *et al.* 1995). It occurs only at very low flow rates when the rivulet is thin and narrow and will not be scrutinized in detail here.

https://doi.org/10.1017/S0022112096004879 Published online by Cambridge University Press

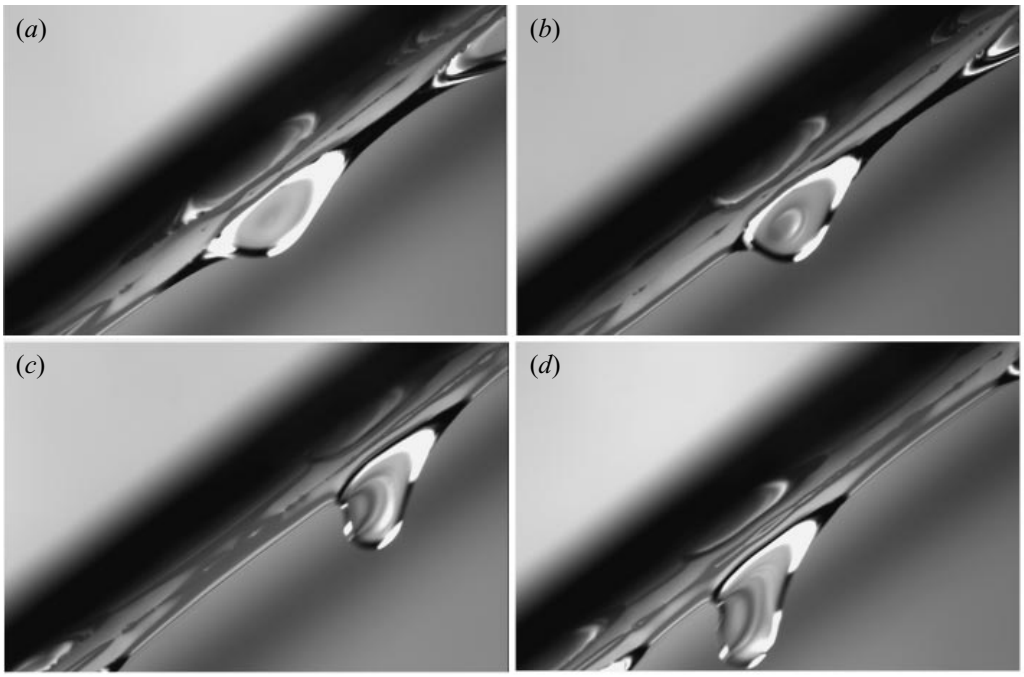


FIGURE 4. Four humps (drops) observed at $\theta = \theta_c$ at various stages of evolution towards pinch-off. They correspond to quasi-steady humps on the hump solution branch with increasing proximity to the critical pinch-off hump solution. The humps steepen and increase their amplitude while their front faces flatten and begin to develop a negative curvature in (*c*) and (*d*). (The conditions are $\theta = 36^\circ \sim \theta_c, q = 1.4$ cm^3 s^{-1} and $\nu = 1.92$ cm^2 s^{-1}.)

A set of recorded raw data for θ_c of the glycerin–water solution is shown in figure 6. The intermediate-flow-rate pinching mechanism yields a distinctly different θ_c dependence on q from the jet mechanism at higher flow rates.

3. Derivation of the lubrication equation

For the flow rates where drop fall-offs are observed in our experiments, the Reynolds number never exceeds unity. This suggests that the inertia instability discovered by Weiland & Davis (1981) for overlying rivulets is not important here. A lubrication approximation which ignores inertia or 'dynamic pressure' is then valid for these low-Reynolds-number rivulets. However, the usual long-wave approximation in a two-dimensional lubrication approximation also requires that the normal scale in y or the interfacial height be smaller than the tangential length scales x (downstream coordinate) and z (transverse coordinate). Our subcritical drops ($\theta > \theta_c$) have very gentle slopes in profile and hence the long-wave approximation in x is valid. However, critical drops near fall-off often have very steep front faces (figures 3 and 4) with slopes of unit order. Moreover, the static contact angle φ is in excess of 45° which also implies that the long-wave approximation in z is questionable.

A possible remedy to the above problem is to retain the full curvature expression in the lubrication analysis (Rosenau *et al.*, 1992) While the 'regularization' is incompatible with some of the other long-wave approximations made in the derivation of the Benney-type lubrication equation, Rosenau *et al.* have shown that they suppress the blow-up behaviour observed in the usual Benney equation for overlying films with

https://doi.org/10.1017/S0022112096004879 Published online by Cambridge University Press

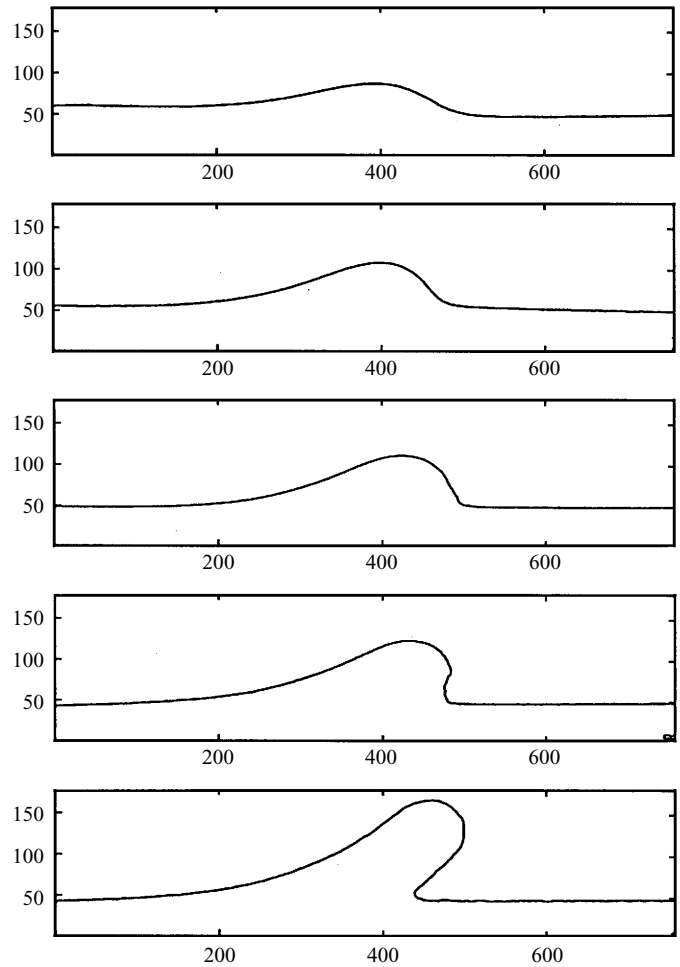


FIGURE 5. Profiles of drops at $\theta = \theta_c$ for the pinch-off mechanism, showing the flattened front face and the overhang with a two-dimensional necking pendent drop cross-section. (The conditions are $\theta = 45^\circ \sim \theta_c, q = 2.27$ cm^3 s^{-1} and $\nu = 2.18$ cm^2 s^{-1}.)

inertia where such behaviour is obviously not physical. (Large structures that violate the long-wave approximation have never been observed for overlying films at low Reynolds numbers.) However, drops do fall off from a pendent rivulet and we expect blow-up to also occur for a 'regularized' lubrication equation which retains the full curvature expression, although it may occur under more severe conditions than the long-wave equation. Since the latter is much easier to analyse, we prefer to use it in our analysis but our result will be a necessary condition for blow-up. To examine how close this necessary condition is to the exact condition, we shall compare our approximation solution to a particular solution which retains the full curvature and to actual near-critical drops. We shall show that the x-expansion faithfully captures the slope of the front face and the curvature of the back face of the drop, the most important features of the solution, even though the expansion is strictly invalid there. For the long-wave z-expansion, drop fall-off is dominated by the force balance along the centreline of the pendent rivulet where the gravitational head is largest. The azimuthal slope h_z and the curvature are indeed small here along the centreline and a

https://doi.org/10.1017/S0022112096004879 Published online by Cambridge University Press

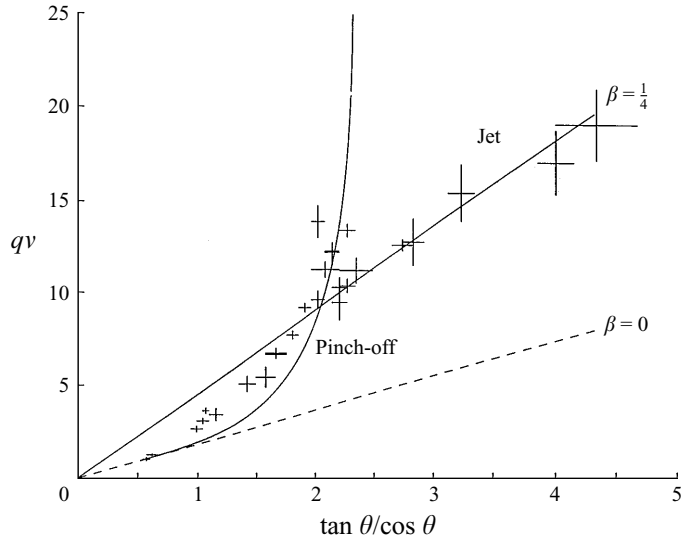


FIGURE 6. A typical set of fall-off data for the glycerin–water solution with error bars attached. The jet asymptote $\beta = 1/4$ and the limiting $\beta = 0$ pinching asymptote are shown. Both are used to determine the static contact angle φ.

long-wave approximation can be made. We shall assume that this approximation can be extended to the contact lines where $h_z \sim \tan\varphi$ is of unit order and the approximation is strictly invalid. While the resulting cross-section profile is definitely in error near the contact lines, the flow rate and the fall-off mechanism are faithfully captured since both are dominated by the flow near the centreline. Analysis without invoking this lubrication approximation is simply too complex since the outer drop solution corresponds to a three-dimensinal solution of the full Laplace–Young equation. Even numerical solution with a boundary condition that varies along the contact line, due to matching with the inner rivulet solutions, is extremely difficult. Some justification of this approximation was offered by Rothrock (1968) who found the straight-rivulet flow rate obtained by the long-wave theory to be close to the measured ones. This will again be verified by our experimental data later in this section. The long-wave approximation in z is actually valid for relatively flat rivulets of more-wetting fluids with small φ. However, we were unable to find a convenient fluid for our experiments that has a small φ.

With the above assumption, a full lubrication equation for flat rivulets with reflection symmetry across the centreline can be derived with the usual long-wave expansion (see Joo *et al.* 1991*a*, for example). It yields locally parabolic velocity profiles in the x- and z-directions that are functions only of the normal coordinate y and the local interfacial height $h(x, z, t)$. The latter dependence comes from the interfacial normal stress jump condition containing the capillary effect. The curvature

$$\kappa = -\frac{h_{xx}(1+h_z^2) + h_{zz}(1+h_x^2) - 2h_x h_z h_{xz}}{(1+h_z^2+h_z^2)^{3/2}}$$

for the capillary term is approximated by the usual long-wave expansion $\kappa \sim -(h_{xx} + h_{zz})$ as explained earlier. The film-averaged kinematic condition then yields the

https://doi.org/10.1017/S0022112096004879 Published online by Cambridge University Press

required lubrication equation

$$\frac{\partial h}{\partial t} + \frac{g \sin\theta}{3\nu}(h^3)_x + \frac{g \cos\theta}{3\nu}\nabla \cdot (h^3 \nabla h) + \frac{\sigma}{3\mu}\nabla \cdot (h^3 \nabla^3 h) = 0, \tag{3.1}$$

where $\nabla = (\partial/\partial x, \partial/\partial z)^T$ is the two-dimensional del operator. The second term represents the front-steepening, gravity-driven tangential mean-flow term while the third and fourth terms represent flows induced by the destabilizing gravitational pull in the y-direction normal to the plane and the stabilizing capillary force respectively.

Equation (3.1) admits a uniform rivulet solution governed only by gravity and the azimuthal capillary force,

$$h^*(z) = \frac{H \tan\varphi}{\sin B}[\cos(z/H) - \cos B], \tag{3.2}$$

where $H = (\sigma/\rho g \cos\theta)^{1/2}$ is the capillary length specified by surface tension and the normal gravity pull and φ is a static contact angle. The parameter B is the half-width of the rivulet scaled with respect to H. The cross-section of the rivulet is hence a segment of the cosine curve. For $B = \pi/2$, the contact lines lie exactly along the zeros of the cosine curve. The value of B can vary from 0 to π and is defined by the requirement that a continuous mean flow, fed from the top of the plane, flows down the x-direction.

This straight-rivulet solution hence involves only a static cross-section satisfying a long-wave two-dimensional Laplace–Young equation in y and z. With a specified contact angle φ, there is a family of these solutions parameterized by the rivulet half-width B, and B must then be determined by stipulating that the flow through the rivulet is consistent with the feed flow rate. From the original parabolic lubrication approximation of the velocity profile, the flow rate q through this rivulet is

$$q = \frac{2g}{3\nu}\left(\frac{\sigma}{\rho g}\right)^2 \frac{\tan\theta}{\cos\theta}\left(\frac{\tan\varphi}{\sin B}\right)^3 \int_0^B (\cos z - \cos B)^3 \mathrm{d}z, \tag{3.3}$$

where z in (3.3) is the dimensionless version scaled by H. Note that (3.2) and (3.3) hold only for the case of partially wetting fluid. For the special case of a completely wetting fluid, $B = \pi$ and the static straight-rivulet solution becomes

$$h^* = \left(\frac{3}{5\pi}\frac{\nu}{g(\sigma/\rho g)^{1/2}} q \frac{\cos^{1/2}\theta}{\sin\theta}\right)^{1/3} (\cos(z/H) + 1). \tag{3.4}$$

In the analysis below we shall only consider the case of partial wetting.

The full Laplace–Young equation with full curvature for the cross-section of a straight rivulet can be solved without considerable effort. A computed profile with the same height h_{max} and contact angle $\varphi = 50^\circ$ as the long-wave approximation (3.2) is compared to the latter in figure 7. It is evident that the profile near the centreline where the slope is gentle is faithfully captured by the simple expression while the profile near the contact line, including the width, is not estimated well. However, since fall-off occurs from the centreline, we expect our estimate of blow-up from the long-wave equation to be an accurate one. Since most of the flow is also near the centreline, we have also compared (3.3) to the flow rate calculated from a cross-section governed by the full Laplace–Young equation in figure 8 for various values of h_{max} and φ. For the regions of interest in this analysis, (3.3) is accurate to within 5% of the solution with the full curvature in z. This partially justifies the long-wave expansion in z but the accuracy of our estimate must still await a comparison to experimental data.

https://doi.org/10.1017/S0022112096004879 Published online by Cambridge University Press

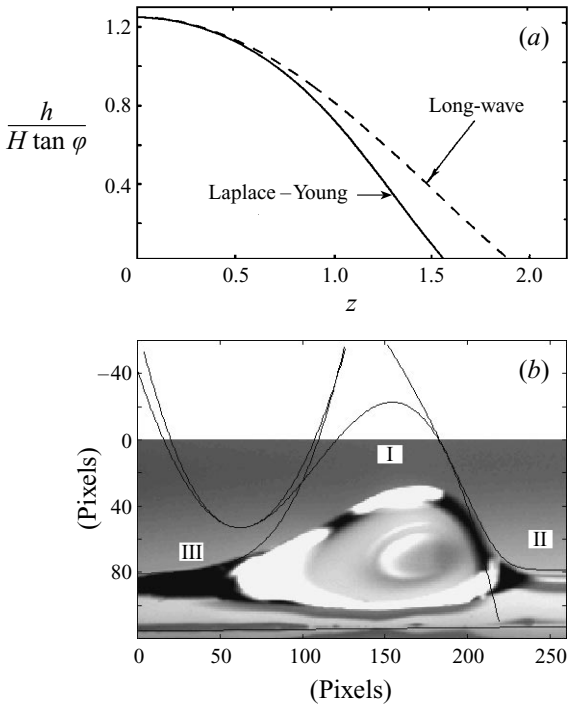


FIGURE 7. Examination of the long-wave approximation. In (*a*), the cross-section profile of a straight-rivulet equation from a long-wave approximation in z and from the full Laplace–Young equation for the same rivulet height h_{max} and same static contact angle φ are shown. While the width B of the rivulet and the profile near the contact line are poorly captured by the long-wave approximation, the curvature at the centreline where fall-off occurs is accurately captured. In (*b*) the drop and rivulet solutions from our matched asymptotic analysis are compared to a photographed drop of the same length (34 pixels = 0.3 cm). While the drop amplitude is not captured by solution I of the long-wave expansion in x, the slope of the front face and the curvature of the back, which are required for the matched asymptotic analysis, are captured by solutions II and III respectively.

We find it convenient to scale x and z by H and h by $(H \tan\varphi / \sin B)$ even though these are not necessarily the natural length scales for the various regions in figure 7. Nevertheless, the straight-rivulet solution (3.2) now becomes simply

$$\xi(z) = \cos z - \cos B \tag{3.5}$$

which is a segment of the cosine curve symmetric about the centreline $z = 0$. The half-width of this normalized straight rivulet is B, its height $\xi_0 = \xi(0)$ is $1 - \cos B \equiv 1 + \beta$ and its dominant centreline azimuthal curvature is -1. The straight rivulet is hence conveniently represented by the parameter B or $\beta = -\cos B$ in this representation where B varies only from 0 to π and β from -1 to 1. We shall associate the critical condition to β and show that drops do not fall off rivulets with flow rates corresponding to β between 0 and $1/4$, a rather narrow range such that $\cos B$ is essentially zero and $\sin B$ unity. The cross-section of the straight rivulets at these particular limits correspond to symmetric cosine curves. The base line of the former ($\beta = 0$) connects the two zeros of the cosine function and while the latter has only a slightly larger base line. We shall exploit the fact that β is small ($\beta < 1/4$) within these limits to carry out an expansion in β.

Note that a uniform rivulet has no natural length scale in the x-direction. Due to

https://doi.org/10.1017/S0022112096004879 Published online by Cambridge University Press

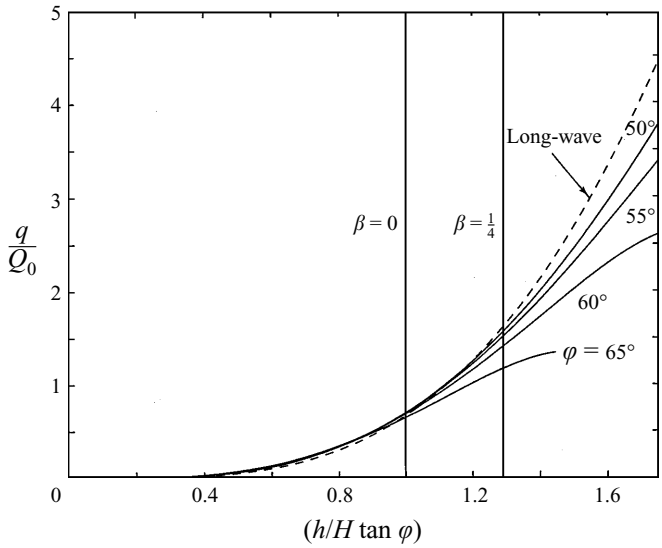


FIGURE 8. The straight-rivulet flow rate from the full Laplace–Young equation and from the long-wave approximation at various contact angles φ. Within the domains of interest between $\cos B = 0 (\beta = 0)$ and $\cos B = -1/4 (\beta = 1/4)$ and $\varphi = 50°$ to $70°$, the long-wave approximation yields an estimate of the flow rate to within 5%.The flow rate is scaled by $Q_0 = (2/3)(g \sin\theta/\nu)H^4 \tan^3\varphi$.

the stabilizing effect of the azimuthal curvature, the phase speed and the growth rate of the most unstable 'normal mode' disturbances are smaller than those for a flat film with the same flow rate per unit width and the wavelength of such disturbances is several times larger than the flat film value of $2\pi\sqrt{2}H$. But because we are interested in a large-drop solution with a large variation of scales across the drop, we shall keep this scaling x for now. The actual length scales for different parts of the drop will be determined later.

Equation (3.1) hence becomes, after the scaling,

$$\alpha\xi_0^2\frac{\partial h}{\partial t} + \alpha(h^3)x + \nabla\cdot(h^3\nabla[h + \nabla^2 h]) = 0 \tag{3.6}$$

where $\alpha = \sin B \tan\theta/\tan\varphi$ and time has been scaled by H/U where

$$U = \left(\frac{gH^2\sin\theta}{3\nu}\right)\left(\frac{\tan\varphi}{\sin B}\right)^2\xi_0^2$$

is the characteristic velocity within the rivulet (U is equal to 2/3 of the maximum liquid velocity). The problem is hence parameterized by two parameters α and $\beta = -\cos B$. For a given fluid at a particular flow rate q and inclination angle θ, the continuous mean-flow expression (3.3) defines a unique pair of β and α. The uniform-rivulet solution is unstable for some flow rates and inclination angles (or α and β). We shall determine whether the mean-flow and capillary stabilizing effects allow a large-drop solution to exist instead. When the gravitational pull exceeds these effects such that a feasible drop solution ceases to exist, the fall-off phenomenon ensues. In general, α can vary from zero to infinity. However, in the pertinent range of small β, α is either a small number or a number of unit order. We shall also expand α in some power of β. This leaves only one small parameter β for the entire problem.

https://doi.org/10.1017/S0022112096004879 Published online by Cambridge University Press

As the straight rivulet destabilizes, our experiments show that its width B remains constant for a particular flow rate and θ while the height grows into localized drops. The contact-line resistance at the edge of the rivulet is simply too large for it to expand widthwise. Kinematic considerations in the scaling arguments of §1 dictate that the initial speed of the growing drop scales as the square of the drop amplitude. There is hence a rapid acceleration as the drop grows. However, when the drop grows to an amplitude much larger than the rivulet height in front and behind it (see figure 4), the speed of the drop is determined by how fast fluid drains in and out of the back and front rivulets, respectively. Because of the large difference in the scales across the drop, capillarity becomes as important a driving force for flow as gravity. Hence, the h^2 kinematic wave speed by considering gravity alone becomes invalid. Capillarity also arrests the gravity-driven growth of the drop such that a steady drop which translates at a constant velocity c is reached eventually, if fall off does not occur.

We hence seek a steady solution to (3.6) in a frame moving with speed c,

$$-\alpha c\xi_0^2 h_x + \alpha(h^3)_x + \nabla\cdot(h^3\nabla(h+\nabla^2 h)) = 0 \tag{3.7}$$

with the condition that a straight rivulet is reached at the two infinities

$$h(x\to\pm\infty) = \xi(z). \tag{3.8}$$

As is consistent with the approach described in §1, we seek the limits when a physically feasible finite-amplitude drop solution to (3.7) and (3.8) becomes impossible in the following analysis and associate them to the fall-off conditions.

4. Matched asymptotic analysis

Solution of (3.7) with boundary conditions (3.8) is difficult both numerically and analytically. However, we are aided by the observation that the near-critical steady-travelling saturated drops in our experiment have several very different length scales as do all localized solutions. In the middle of the drop, the drop height is so large that viscous effect becomes unimportant and the drop is essentially a static one with steepening due to the mean-flow effect. Away from the drop, however, the interfacial height decays very rapidly to that of the straight rivulet in (3.5) which is about 3 to 5 times smaller. With this drastic reduction in amplitude, the gravitational head in the normal direction becomes negligible and the dominant forces are now capillary and viscous forces. As a result, the equation can be simplified and becomes partially solvable at the drop and at the front and back rivulets. The solutions can then be matched to yield an estimate of the full solution and to determine the latter's existence. This matched asymptotic expansion is analogous to the matching of thin-film inner solutions to static outer solutions in the studies of steady replacement of liquid by air in a capillary (Bretherton 1961) and steady drops sliding on a coated wire (Kalliadasis & Chang 1994). The present matched asymptotic problem has the complexity of an additional dimension and our matching will not yield a closed-form solution. However, the existence of the final solution can still be estimated to offer convenient fall-off criteria.

One welcome simplification of the pertinent partial differential equation is that it can sometimes be reduced to an ordinary differential equation like the one studied by Bretherton (1961) and Kalliadasis & Chang (1994) with a similarity transform. This self-similarity is based on the observation that the cross-section of the back rivulet resembles that of a straight rivulet. Since the rivulet width remains the same,

https://doi.org/10.1017/S0022112096004879 Published online by Cambridge University Press

this suggests the back-rivulet solution is simply the straight-rivulet solution (3.5) multiplied by an amplitude modulation f which is mostly a function of x only.

The large amplitude of the drop in region I in figure 9 relative to those of the straight rivulets suggests that the viscous shear term $-c\alpha\xi_0^2 h_x$ in (3.7) is negligible within the drop. However, the steepened asymmetric drop shape seen in figure 4 indicates that the mean-flow term $\alpha(h^3)_x$ must be of the same order as the capillary and gravity terms. This mean-flow term is the same as the tangential gravity term in a static drop and upon integrating (3.7) once, we get the long-wave Laplace–Young equation in the moving coordinate for the static drop under an inclined plane

$$\alpha x + h + h_{xx} + h_{zz} = A, \tag{4.1}$$

where A is an integration constant, with boundary conditions $h(z = B) = h_z(z = 0) = 0$ to ensure constant width and reflection symmetry in z. The mean-flow term gives rise to the αx-term which represents hydrostatic head in the tangential x-direction here.

While (4.1) corresponds to a long-wave static Laplace–Young equation, its dimensional length scales are not just the capillary length scale H such that $x \sim O(1)$ from scaling. This is because of the slender geometry of the rivulet and the cross-section shape (3.5) which stipulate a different length scale. We shall show that the back-rivulet solution is of the form $h(x, z) = \xi(z)f(x, z)$ where $f(x, z)$ is mostly a function of x. As a result, for the solution of (4.1) to match the front solution, the normal gravitational term and the axial curvature term must be of order

$$h + h_{zz} \sim f(\xi_{zz} + \xi) = \beta f\xi = \beta h.$$

Hence, balancing βh with αx and h_{xx}, the tangential gravitational term in (4.1), we obtain the horizontal scale x and the normal scale h for the static drop region

$$x \sim O(|\beta|^{-1/2}), \qquad h \sim O(\alpha|\beta|^{-3/2}), \tag{4.2}$$

where α and β are both small parameters. Bounds on the relative order of α and β can be obtained by observing that h must be in excess of the unit amplitude of a straight rivulet,

$$\alpha = |\beta|^n, \qquad 0 < n < 3/2.$$

The lower bound on n is due to the fact that α is at most unit order. A more precise estimate of n will be introduced by the assumptions we make to render the rivulet equations solvable. Scalings (4.2) also stipulate that $h_x \sim \alpha|\beta|^{-1}$ must be much larger than $h_{xx} \sim \alpha|\beta|^{-1/2}$. This is the steepening effect of the mean-flow term (the tangential gravitation term) which renders the front profile of the drop nearly linear as seen in figures 4, 5, 7 and 9. The back profile, however, remains curved and is tangent to the rivulet in the figures. This implies that the front and back scalings are entirely different in the matching regions II and III.

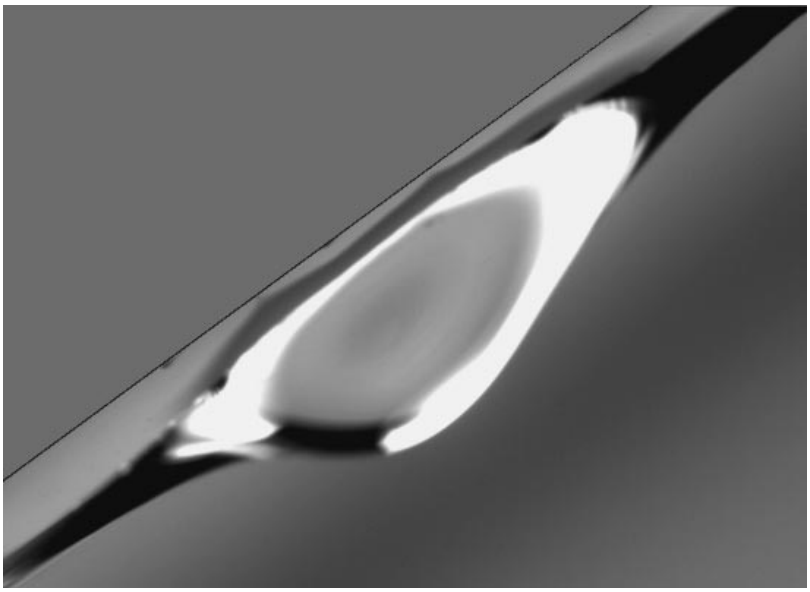
The drop solution to (4.1) in region I can be obtained by eigenfunction expansion,

$$h_d(x, z) = \frac{A - \alpha x}{\beta}\xi(z) + \sum_{n=0}^{\infty} \cos(\lambda_n z)[C_n \sinh(\lambda_n^2 - 1)^{1/2}x + D_n \cosh(\lambda_n^2 - 1)^{1/2}x], \tag{4.3}$$

where $\lambda_n = (\pi/B)(n + 1/2)$. Coefficients A, C_n and D_n are unknown and remain to be determined from matching with the front- and back-rivulet solutions.

Since the rivulet width is constant across regions I to III where the variation in x has been assumed to be gradual and since the dominant term in the drop solution (4.3) in region I has a cross-section $\xi(z)$ of a straight rivulet (3.5), we expect the front-

https://doi.org/10.1017/S0022112096004879 Published online by Cambridge University Press



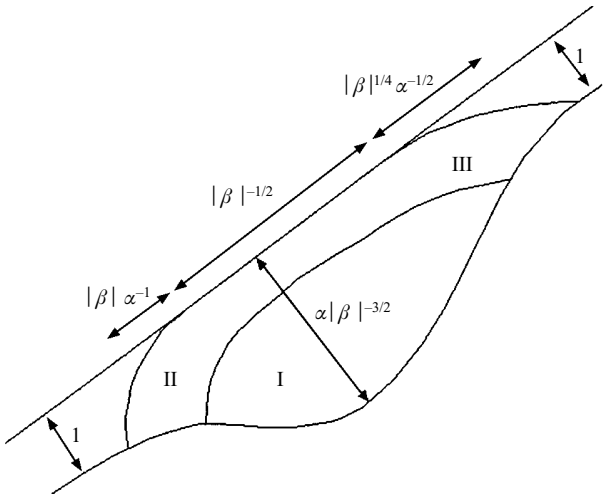


FIGURE 9. The various regions of a steady hump length scales relative to the straight rivulet with unit height. Region I is the static drop region, region II is the front matching region where the large slope is of order $\alpha|\beta|^{-1}$ and region III is the back matching region where the slope vanishes and the centreline curvature is of order $\alpha|\beta|^{-1/2}$

and back-rivulet solutions in regions I and III to have the form $h = \xi(z)f(x,z)$ such that the amplitude $f(x,z)$ approaches unity gradually at $x = \pm\infty$ as the straight front and back rivulets are approached. The envelope function $f(x,z)$ describes how the rivulet amplitude varies near the centreline. It captures the long-wave axial curvature

$$h_{xx} = \xi f_{xx}, \tag{4.4}$$

but for the long-wave azimuthal curvature,

$$h_{zz} = \xi_{zz} f + 2\xi_z f_z + \xi f_{zz}, \tag{4.5}$$

https://doi.org/10.1017/S0022112096004879 Published online by Cambridge University Press

it shows, in addition to the straight-rivulet azimuthal curvature ξ_{zz}, the contributions from the cross-rivulet variation of the envelope. Such variations arise from the terms in the infinite series of the drop solution (4.3) in region I. They hence become important in the matching regions II and III where the front- and back-rivulet solutions meet the drop solution (4.3). (At $x \to \pm\infty, f$ approaches unity as the straight-rivulet solution is again approached.) The three-dimensional structure of the drop requires the matching to occur along matching lines $x_f(z)$ and $x_b(z)$ across the centreline. In addition, the asymmetric shape of the drop solution (4.3) due to gravity steepening stipulates the relative dominance of ξ_{zz} and f_{zz} in the two regions and provides different governing equations for $f(x,z)$. Such relative dominance is also reflected in the width of the two matching regions around $x_f(z)$ and $x_b(z)$ and this, in turn, simplifies the equations for f to the extent they can be studied analytically.

The governing equation for the back rivulet in region III is especially simple. In this region, the rivulet amplitude is that of a straight rivulet and hence $h \sim f \sim O(1)$. The matching occurs in some neighbourhood of the matching line $x_b(z)$. Because of the limitation of our long-wave approximation in z, as is evident in figure 7, we shall only carry out the matching near the centreline at $z = 0$. As is seen from the discussion of the drop solution (4.3) in region I, the back profile of the drop is tangent to the straight-rivulet solution in the matching region III. As a result, h_{xx} is much larger than h_x which is the opposite of the case in the front matching region. Since the curvature of the drop solution (4.3) in region I is $\alpha|\beta|^{-1/2}$, this dominant matching specifies that the width of the matching region around $x_b(z)$ is $\alpha^{-1/2}|\beta|^{1/4}$ since $h \sim f$ is of unit order here. We shall require this width to be smaller than unity for our simplified rivulet analysis to be valid. This yields $\alpha = |\beta|^n$, $0 < n < 1/2$. This estimate of the relative order n then replaces the previous upper bound of $3/2$. This scaling for the width of matching region III is indicated in figure 9. We also note that since curvature is dominant in this back-rivulet region, the flow is driven by capillarity and a stationary rivulet can only exist if the axial capillary term $(h^3 h_{xxx})_x$ in (3.7) matches the viscous term $-\alpha c \xi_0^2 h_x$. Since ξ_0 and h are of unit order in region III, this yields another estimate of the x-scaling $(\alpha c)^{-1/3}$ which combines with the former to yield

$$c \sim \alpha^{1/2} \beta^{-3/4}. \tag{4.6}$$

Since $\alpha \sim |\beta|^n$ with $0 < n < 1/2$, this implies that the drop speed c must be larger than unit order to provide sufficient viscous dissipation to balance the capillary effect.

Based on the above scaling arguments for the back rivulet, we define a local unit order coordinate around $x_b(z)$

$$\eta = \frac{x - x_b(z)}{\Gamma(z)}, \tag{4.7}$$

where $\Gamma(z) \ll 1$ is the width of order $(\alpha c)^{-1/3}$ and $x_b(z)$ is of unit order since the origin of the static drop (4.3) is at the front, $x_f(0) = 0$, and the drop has unit length. Hence, the decomposition $h_b(x,z) = \xi(z) f(\eta)$ yields

$$h_z = \xi_z f - \left(\frac{\mathrm{d}x_b}{\mathrm{d}z} + \eta \Gamma_z\right) \xi f_\eta / \Gamma \approx -\left(\frac{\xi f_\eta}{\Gamma}\right)\left(\frac{\mathrm{d}x_b}{\mathrm{d}z}\right), \tag{4.8}$$

where the order assignment of unit order ξ, η, z and x_b has been invoked. In essence, this shows that the variation in the cross-rivulet z-direction near the back rivulet is dominated by the variation in the envelope function f and not the azimuthal curvature of the straight-rivulet solution $\xi(z)$. This is also obvious from the sketch of $x_b(z)$ in figure 9 which is almost tangent to the centreline x-axis. In contrast, $x_f(z)$

https://doi.org/10.1017/S0022112096004879 Published online by Cambridge University Press

in the front matching region II is almost perpendicular to the centreline. Substituting $h_b(x,z) = \xi(z)f(\eta)$ into (3.7), retaining leading-order terms in the matching region III, which leaves only the viscous term and the capillary term, and invoking the fact that the variation in z along the matching region is dominated by $f(\eta)$ instead of $\xi(z)$ as shown in (4.8), we find that the p.d.e. (3.7) collapses to an o.d.e. due to the approximate similarity transform (4.7). This occurs because both the x- and z-dependence are captured by the envelope function $f(\eta)$ and the cross-section $\xi(z)$ can be factored out as if it were a constant. In particular, $h_{zz} \sim \xi f_{zz}$ in (4.5). Geometrically, it implies that along the matching line $x_b(z)$, the changes in the azimuthal curvature arise mostly from the z-variation of the envelope function and not the variation in $\xi(z)$ – the line $x_b(z)$ is nearly parallel to the centreline.

Not surprisingly, the resulting o.d.e. for the amplitude function which balances axial curvature and viscous dissipation is the Bretherton equation for capillary-driven flow (Bretherton 1961),

$$-f_\eta + [f^3 f_{\eta\eta\eta}]_\eta = 0 \tag{4.9}$$

with the condition $f(\eta \to -\infty) = 1$. From the classical results of Bretherton and the more accurate approach of Kalliadasis & Chang (1994), we choose an initial condition in the integration of (4.9) such that f blows up quadratically and the limiting linear term vanishes exactly, as required by the drop solution

$$\lim_{\eta\to\infty} h_b(\eta(x,z)) = \xi(z)[\tfrac{1}{2}\hat{a}\eta^2 + \hat{c}], \tag{4.10}$$

where $\hat{a} = 0.64304$ and $\hat{c} = 2.897$. We shall match this back solution to the drop solution (4.3) along a local expansion of $x_b(z)$ about the centreline

$$x_b(z) \sim -x_b^0 + \tfrac{1}{2}\kappa_b z^2, \tag{4.11}$$

where κ_b is the positive transverse curvature of the back face representing convexity and the origin of the centreline is chosen to be the tip of the front matching line $x_f(z)$, to be introduced later. We shall require the transverse curvature and the normal derivatives to match here as in the classical Bretherton matching (Bretherton 1961)

$$\nabla^2(h_b - h_d)|_{x=x_b(z)} = 0, \tag{4.12}$$

$$\left(\frac{\partial}{\partial x} - \frac{\mathrm{d}x_b}{\mathrm{d}z}\frac{\partial}{\partial z}\right)(h_b - h_d)|_{x=x_b(z)} = 0. \tag{4.13}$$

Matching of the height is not carried out, because it occurs at a higher order.

Consider now the front region II. The steepened front of the drop implies that the matching in front should be the dominant height and the normal derivative since the curvature is small. Consequently, the scalings (4.2) for region I imply that the normal derivative of the front region II should be of order $\alpha|\beta|^{-1}$. The only compatible scalings are then $z \sim O(1), h \sim O(1)$ and

$$x \sim O(|\beta|\alpha^{-1}) \tag{4.14}$$

which is small as $\alpha \sim |\beta|^n$ where $0 < n < 1/2$. Comparing (4.14) to (4.2) and (4.8), it is clear that the length of the front matching region II is much shorter than that of the back region III due to the steepened front. The length scales of all three regions are shown in figure 9.

If we choose the origin in x to be the front edge of the drop solution (4.3), then the front matching line $x_f(z)$ also begins at $x = 0, x_f(0) = 0$. Because the dominant derivative for the drop solution in this region is $h_x \gg h_{xx}$, the drop interface has a

https://doi.org/10.1017/S0022112096004879 Published online by Cambridge University Press

nearly linear slope with respect to x in this region as seen in figure 9. We shall hence discard the axial curvature term $(h^3 h_{xxx})_x$ in (3.7) for this front matching region. If one decomposes $h_f = \xi(z)g(x,z)$ as before, this implies that g does not vary much along the front matching line $x_f(z)$. This is supported by a matching region that is almost perpendicular to the centre axis in figure 9 – the envelope function $g(x,z)$ does not vary much within this narrow band. Consequently, we choose the opposite of what we have done for the back – the variation in z of h_f is concentrated in $\xi(z)$

$$h_z \sim \xi_z f, \quad h_{zz} \sim \xi_{zz} f,$$

which simplifies (4.5). Although the higher curvature term $(h^3 h_{xxx})_x$ can be omitted from (3.7) in this front matching region, the rapid linear rise in the rivulet amplitude implies that, unlike the back rivulet, the mean-flow term $\alpha(h^3)_x$ and the gravitational term $\nabla\cdot(h^3\nabla h)$ should still be retained. We shall also not carry out an explicit scaling of the matching region as in (4.7) abut simply substitute $h_f = \xi(z)g(x,z)$ into (3.7) and neglect all z-derivatives of $g(x,z)$ to obtain the back-rivulet equation

$$-(\alpha c)\xi_0^2\xi g_x + \alpha\xi^3(g^3)_x + \xi^3\beta[g^3 g_x]_x + g^3 g_{xx}(\xi^3\xi_z)_z = 0. \tag{4.15}$$

Unlike (4.9), the p.d.e. (3.7) does not collapse into an o.d.e. Nevertheless, (4.15) is an o.d.e. for g in x with coefficients that are dependent on z. Analytic estimate of the solution to this equation is far simpler than a p.d.e. It should be solved with the condition that $g(x\to\infty,z)=1$.

The decomposition of h_f into $\xi(z)$ and $g(x,z)$ requires further scrutiny. Letting $g(x,z) = 1+\psi(x,z)$ and expanding (4.15) to linear order in ϕ, we obtain

$$\psi_x = -\frac{\alpha p}{\beta}\left[\frac{c\xi_0^2}{3\xi^2} - 1\right]\psi, \tag{4.16}$$

where

$$p(z) = \frac{3\beta\xi}{\xi(\xi-2\beta) - 3\xi_z^2}. \tag{4.17}$$

The condition that ψ_x must be negative such that the rivulet can grow from the straight rivulet to the drop in the $-x$-direction then requires that $c>3$ (since the centreline amplitude ξ_0 is larger than $\xi(z)$) and $p(z)/\beta > 0$. The first condition is always satisfied since $(\alpha c)^{2/3} \sim \alpha/|\beta|^{1/2} \gg 1$, which implies that $c \gg 1$ since α is order unity or smaller. The second condition $p(z)/\beta > 0$ is satisfied if $\cos z > 0.5(3+\beta^2)^{1/2}$. This implies that the decomposition is only valid in some neighbourhood of the centreline at $z=0$ where the lubrication expansion is most correct. We shall hence expand in z to $O(z^2)$ and match the solutions to this order in z only. This is consistent with the expansion of the back matching line in (4.11). Because our representation of the front-rivulet solution holds only near the centreline, we shall focus first on the centreline such that $p=p_0$ and $\xi=\xi_0=1+\beta$. We note that the width B increases with increasing β, representing higher gravitational pull. The value $\beta=0$ corresponds to a rivulet cross-section that is exactly the top half of the cosine function.

Because a similarity transform that reduces the back-rivulet equation to (4.9) does not exist here for the front-rivulet since the scalings do not permit omission of terms that allow a self-similar transform, we shall need to solve for $g(x,z)$ at every z-position or, more precisely, to $O(z^2)$ about the centreline. We do so by writing (4.15) as

$$(g^{-p}g_x)_x = -\frac{\alpha}{\beta}[(g^{-p})_x - \frac{cp}{3(p+2)}\left(\frac{\xi_0}{\xi}\right)^2 (g^{-p-2})_x]. \tag{4.18}$$

https://doi.org/10.1017/S0022112096004879 Published online by Cambridge University Press

We note that $p(z) = -3$ if ξ is constant and it is the azimuthal curvature of the rivulet cross-section $\xi(z)$ that renders $p(z)$ a function of z. Even at the centreline, $p(z=0) = p_0 = 3\beta/(1-\beta)$ is not -3 due to the azimuthal curvature. The behaviour of g as $x \to -\infty$ is determined entirely by $p(z)$. The asymptotic behaviour of (4.18) at the centreline as $x \to -\infty$ and $f \to \infty$ can be readily obtained. For $p_0 > 0$, one obtains

$$g \sim \left[g_0^{1-p_0} + \frac{\alpha}{\beta}(1-p_0)\left(\frac{cp_0}{3(2+p_0)} - 1\right)(x_0 - x)\right]^{1/(1-p_0)}, \tag{4.19}$$

where x_0 and g_0 are arbitrary reference points. It is then clear that g blows up at

$$x_\infty = x_0 - g_0^{1-p_0} / \left[\frac{\alpha}{\beta}(p_0 - 1)\left(\frac{cp_o}{3(p+2)} - 1\right)\right] < x_0$$

if $p_0 > 1$ or equivalently, $\beta > 1/4$. For $0 < p_0 < 1$ where

$$0 < \beta < 1/4 \quad \text{or} \quad \pi/2 = 1.571 < B < 1.824 \tag{4.20}$$

$g(x,0)$ grows continuously to infinity in the power $|x|^{1/(1-p_0)}$ as x approaches negative infinity. For $p_0 < 0$ or $\beta < 0$, g does not grow to infinity at all but saturates at a constant value as x approaches $-\infty$. To allow matching with the drop solution h_d, f must grow to infinity and this rules out the case of negative β. However, it must grow in such a manner that it can match with the drop solution whose curvature is small. This can never happen for $\beta > 1/4$ when f grows as $|x - x_\infty|^{-\sigma}$ where $\sigma = 1/|p_0 - 1|$. When g is large in this case, g_{xx} is much larger than g_x which is distinctly different from the behaviour at the steepened front of the drop solution h_d.

Hence, front matching is only possible if (4.20) is satisfied. Condition (4.20) yields the surprising result that while the rivulet amplitude can vary over several scales, the normalized rivulet width B, which is independent of z, is bounded within the narrow range (1.571, 1.824)! Since $p_0 = -3$ for a flat film, this also implies that a drop can only be sustained when the azimuthal curvature of the rivulet is present. Physically, it implies that, unlike the drop region where the normal gravitational pull is countered by both the axial curvature due to gravity steepening and the azimuthal curvature, only azimuthal curvature cancels the gravitational pull in the front rivulet. When β is negative, the gravitational pull is smaller than the azimuthal capillary force and the interface cannot grow to meet the drop solution. When β is in excess of $1/4$, the gravitational pull exceeds the azimuthal capillary force and the interface grows too rapidly to allow matching. In order to get a steady solution in this case, the matching must occur at infinite height. Physically, this means that the drop cannot drain sufficient fluid into the front rivulet to sustain a steady configuration. The drop will continue to grow since it is still sucking liquid from the back rivulet and it will fall off from the rivulet as a jet. This is the jet mechanism at high flow rate and it occurs at $\beta = 1/4$ or $B = 1.824$ of condition (4.20). The effect of gravity steepening in increasing the front normal curvature of the hump in (4.3), which we have yet to resolve, and preventing further growth due to gravity can only be successful if (4.20) holds. Otherwise, no amount of gravity steepening can prevent fall-off. It is a necessary condition for a steady drop solution. The critical condition of $\beta = 1/4$ is hence a simple criterion derived from fundamental considerations about the front rivulet.

Even when criterion (4.20) is satisfied, the existence of the drop solution is not guaranteed. All the matching conditions must be satisfactorily met to allow the complete construction of the entire drop spanning the various scales of the drop and

https://doi.org/10.1017/S0022112096004879 Published online by Cambridge University Press

front and back rivulet sections. Since the front-rivulet equation does not collapse into an ordinary differential equation like the Bretherton equation for the back, it must be solved explicitly in both x and z. To this end, we expand the front matching locus about $z = 0$ to yield

$$x_f(z) \sim -\kappa_f z^2/2, \tag{4.21}$$

where κ_f is positive and the centre location of this front matching line has been set to zero to affix the origin of the x-coordinate. A similar expansion of the rivulet amplitude $g\ (x, z)$ at the front matching locus yields

$$g(x_f(z)) \sim A_1 + B_1 z^2/2. \tag{4.22}$$

These two expansions add three additional unknowns, κ_f, A_1 and B_1, to the problem. Integrating (4.18) once and invoking the condition that $g = 1$ must be a solution, one obtains

$$g_x = -\frac{\alpha}{\beta}\left\{\left(\frac{cp\xi_0^2}{3(p+2)\xi^2}\right)(g^p - g^{-2}) + 1 - g^p\right\} \sim -\frac{\alpha}{\beta}\{\gamma + \tfrac{1}{2}z^2(\gamma_1 + B_1\gamma_2)\} \tag{4.23}$$

after expanding to $O(z^2)$ where

$$\gamma = \frac{c\beta}{2+\beta}\left(A_1^{p_0} - \frac{1}{A_1^2}\right) + 1 - A_1^{p_0},$$

$$\gamma_1 = \frac{(9+2\beta)}{(1+\beta)(1+\beta/2)}[\gamma + A_1^{p_0} - 1] + p_0\left(\frac{7+\beta}{1-\beta^2}\right)\ln A_1\left[\gamma - 1 + \frac{c\beta}{2+\beta}\frac{1}{A_1^2}\right],$$

$$\gamma_2 = \frac{p_0}{A_1}\left[\gamma - 1 + \frac{c}{3A_1^2}\right]$$

are constants containing unknowns A_1 and c.

The behaviour of the front solution $h_f = \xi(z)g(x, z)$ to $O(z^2)$ near the front matching locus can then be extracted from (4.21), (4.22) and (4.23):

$$\begin{aligned} h_f &\sim (\xi_0 - \tfrac{1}{2}z^2)[g(x_f(z)) + (x - x_f(z))g_x(x_f(z))] \\ &\sim A_1\xi_0 - \tfrac{1}{2}z^2(A_1 - B_1\xi_0) - (x + \kappa_f z^2/2)(\alpha/\beta)\{\xi_0\gamma + \tfrac{1}{2}z^2[\xi_0(\gamma_1 + B_1\gamma_2) - \gamma]\}. \end{aligned} \tag{4.24}$$

The front matching involves only the height and the normal derivative since the curvature is negligible,

$$(h_f - h_d)|_{x=-\kappa_f z^2/2} = 0, \tag{4.25}$$

$$\left(\frac{\partial}{\partial x} - \frac{dx_f}{dz}\frac{\partial}{\partial z}\right)(h_f - h_d)|_{x=-\kappa_f z^2/2} = \left(\frac{\partial}{\partial x} + \kappa_f z\frac{\partial}{\partial z}\right)(h_f - h_d)|_{x=-\kappa_f z^2/2} = 0. \tag{4.26}$$

The drop solution (4.2) can be written as

$$\begin{aligned} h_d = \frac{A - \alpha x}{\beta}\xi(z) + \cos\left(\frac{\pi}{2B}z\right)\left\{C_0 \sin\left[1 - \left(\frac{\pi}{2B}\right)^2\right]^{1/2} x + D_o \cos\left[1 - \left(\frac{\pi}{2B}\right)^2\right]^{1/2} x\right\} \\ + \sum_{n=1}^{\infty} \cos\lambda_n z(C_n \sin h\left(\lambda_n^2 - 1\right)^{1/2} x + D_n \cos h\left(\lambda_n^2 - 1\right)^{1/2} x). \end{aligned} \tag{4.27}$$

Note that B is very close to $\pi/2$. Due to the drop scaling $x \sim |\beta|^{-1/2}$, exponential terms for $n \neq 0$ in (4.27) decay very rapidly. Hence, in order for the amplitude of the drop solution to remain finite terms must vanish to leading order and only near-resonant terms with $n = 0$ should be considered.

https://doi.org/10.1017/S0022112096004879 Published online by Cambridge University Press

This simplifies the drop solution to

$$h_d = \frac{A-\alpha x}{\beta}\xi(z) + \xi_0 \cos\left(\frac{\pi z}{2B}\right)\left\{C\sin\left[1-\left(\frac{\pi}{2B}\right)^2\right]^{1/2}x + D\cos\left[1-\left(\frac{\pi}{2B}\right)^2\right]^{1/2}x\right\}. \tag{4.28}$$

The $O(z^0)$ and $O(z^2)$ terms of the matching conditions (4.12), (4.13), (4.25) and (4.26) then provide eight equations for nine unknowns $A, C, D, c, x_b^0, \kappa_b, \kappa_f, A_1$ and B_1.

Solution of these equations yields a family of drop solutions $h(\alpha, \beta; c)$ parameterized by the speed c for a given set of α and β. It is possible that a unique drop solution exists for a given set of α and β and only one member of the family provided by the leading-order expansion is the true solution. However, the higher-order expansion to break this degeneracy is too tedious to carry out. Instead, we seek an approximate sufficient condition when the entire family of drops becomes physically unrealizable. While this is a sufficient condition, we shall demonstrate using experimental data that it is a very accurate estimate. The reason for this is that the range of c that parameterizes the family is narrow.

For the drops to be feasible, the centreline azimuthal curvature and the transverse curvatures of the back and front edges must obey the following convexity inequalities,

$$h_{zz} \leqslant 0, \quad \kappa_b \geqslant 0 \ \text{ and } \ \kappa_f \geqslant 0. \tag{4.29}$$

With some straightforward but tedious algebra, we are able to show from the eight equations that the first two inequalities are always satisfied while the last one is only satisfied for drops with speeds below a critical speed $c_*(\alpha, \beta)$. This is consistent with the pinching mechanism observed experimentally in figure 4(c and d) where κ_f clearly changes sign when the drops begin to fall off. Capillary pinching develops as soon as the front surface becomes concave such that the cross-section resembles a necking two-dimensional pendent drop. Such a cross-section is beyond the description of our lubrication equation but the reversal of the front curvature is captured.

We are unable to provide an explicit expression for $c_*(\alpha, \beta)$. Instead, an equality $\alpha < F(\beta, (\alpha c)^{2/3}\beta^{1/2}/\alpha)$ is derived in the Appendix for drops with negative front-edge curvature κ_f. A tight upper bound on F is also found in the Appendix for F at large $(\alpha c)^{2/3}$ to yield

$$\alpha = \tan\theta \sin B/\tan\varphi < L(\beta)\beta^{1/6}, \tag{4.30}$$

where $L(\beta)$ is a weak function of β

$$L(\beta) = \frac{4\hat{a}}{3\pi}\left\{\frac{9-\beta}{2Sm}\right\}^{2/3}(1+\beta)^{1/3}(1-\tfrac{3}{2}m\beta)\left\{1+\frac{2(1+\beta)}{3\pi}(1-\tfrac{3}{2}m\beta)\right\}^2. \tag{4.31}$$

Inequality (4.30) together with the constant-flow-rate condition (3.3) give a relationship between flow rate and the critical inclination angle θ_c that is parameterized by β. However, further simplifications can be made. The parameters in $L(\beta)$ are $m = [1-(\pi/2B)^2]/\beta$, $S = [1-(1+\beta)(\pi/2B)^2]/\beta$ and $\hat{a} = 0.6430$ such that $L(0) = 1.5$ and $L(1/4) = 1.2$ – very little variation within the range of interest. The quantity $L(\beta)$ can hence be taken as 1.5. The relative scaling of $\alpha \sim \beta^{1/6}$ is then consistent with the prior estimate of β^n with $0 < n < 1/2$. Over this range of β, $\sin B$ ranges from 1.0 to 0.97 and can be considered to be unity. These simplifications produce a very concise form of (4.30) that parallels (4.20),

$$1.5\beta^{1/6} > \tan\theta/\tan\varphi \tag{4.32}$$

https://doi.org/10.1017/S0022112096004879 Published online by Cambridge University Press

showing a unique $(\tan\theta/\tan\varphi)$ dependence absent in the jet criterion. It is also clear by comparing the two criteria (4.20) and (4.32) that they cross over at approximately $\theta = \varphi$.

In the limit of small β, the pinch-off criterion of (4.32) becomes in dimensional form

$$q > \frac{4}{9}\left(\frac{g}{\nu}\right)\left(\frac{\tan\theta}{\cos\theta}\right)\left(\frac{\sigma}{\rho g}\right)^2(\tan\varphi)^3\left\{1+\frac{9}{8}\pi\left(\frac{\tan\theta}{\tan\varphi}\right)^6\left(\frac{1}{L(0)}\right)^6\right\} \tag{4.33}$$

which can be used to estimate the static contact angle φ if it is not known. In contrast, the jet condition of $\beta > 1/4$ in (4.20) yields

$$q > 1.079\left(\frac{g}{\nu}\right)\left(\frac{\tan\theta}{\cos\theta}\right)(\tan\varphi)^3\left(\frac{\sigma}{\rho g}\right)^2 \tag{4.34}$$

without the distinctive $(\tan\theta/\tan\varphi)^6$ dependence of the pinch-off criterion at small β. The latter is stronger than the jet criterion at small α, corresponding to smaller inclination angles $\theta, \theta < \varphi$. This is consistent with our observation that low-flow-rate fall-off at small θ is via the pinch-off mechanism when the front steepening mechanism is relatively weak.

5. Comparison and discussion

As a final check on the validity of our long-wave equation for near-critical drops with large axial slope, we compare our theoretical prediction of the drop solution in region I of (4.28) and the asymptotic rivulet solutions in regions III and II of (4.10) and (4.24) to an actual drop with θ slightly greater than θ_c in figure 7. The back extrapolation of the back-rivulet solution in region III shows that it captures the axial curvature of the drop solution I. This graphic depiction of matched solutions is similar to that carried out by Bretherton (1961). We use the length of the drop as the final equation to specify all nine unknowns in (4.28). As is evident, while the amplitude of the drop is clearly overestimated by the long-wave approximation and the variation in x is clearly not small, the slope of the front face and the curvature of the back face are well-estimated. Since these are the only quantities used in the matched asymptotic analysis, this suggests our estimates for fall-off are very accurate bounds. Although the long-wave equation cannot capture the full interfacial structure of a drop near fall-off, it captures the all-important cross-section azimuthal curvature and the mean-flow-induced axial steepening that counter the gravitational effects which induce fall-off. The two bounds (4.32) and (4.34) are imposed on the raw fall-off data of figure 6 where the asymptotic behaviour of the critical curve at small flow rate is found to be approximated by the pinch-off criterion (4.33) if a static contact angle of $\varphi = 55^\circ$ is used. The same value also fits the $\beta = 1/4$ jet criterion of (4.34). This is within the acceptable range for the static contact angle of the solution (50° to 70°) and is closer to the receding value as expected. We also note that the limiting pinch-off curve (4.33) simply corresponds to $\beta = 0$ and hence the critical curves are bound between $\beta = 0$ and $\beta = 1/4$ as shown in figure 6. The two curves intersect at $\theta \sim 51^\circ$ for the given contact angle $\varphi = 55^\circ$. The unmistakable $(\tan\theta/\cos\theta)$ dependence of q for the jet mechanism (4.34) is very distinct at high flow rates. We hence use the normalized coordinates suggested by (4.32) and (4.34) to scale all our fall-off data, using the $\beta = 0$ and $1/4$ asymptotes to estimate the static contact angle φ. As seen in figure 10, the scaled data reflect the different scalings of the two mechanisms. There is some cross-over at the transition point at $\theta \sim \varphi$ between the

https://doi.org/10.1017/S0022112096004879 Published online by Cambridge University Press

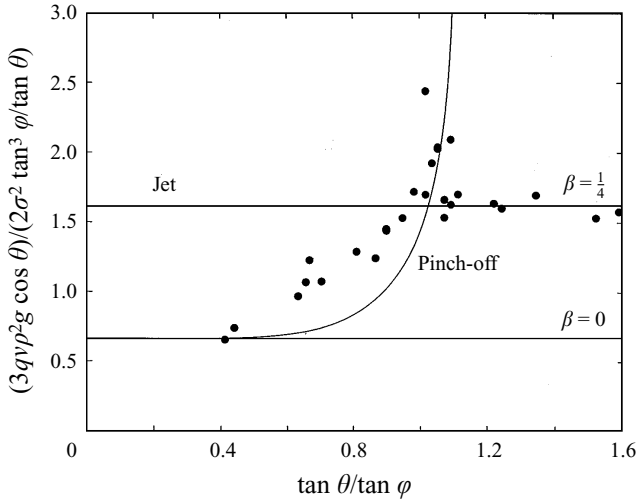


FIGURE 10. The normalized data for the jet and pinch-off mechanisms.

two mechanisms but even the cross-over is well described by (4.32) and (4.34). The viscosity of our glycerin–water solution changes by as much as 25% for the recorded data but we did not vary φ in our experiments. This is becouse of our desire to remove inertia from the fall-off phenomenon. As a result, viscous partially wetting fluids with non-zero receding contact angles are required for realistic experimental conditions. We are unable to find such viscous fluids without introducing viscoelastic effects. Nevertheless, we expect our theory to predict the critical fall-off condition of any non-elastic viscous fluid whose physical properties are known.

This work was supported by grants from DOE and NASA. The original idea was conceived while H.-C. C. was visiting DAMTP, Cambridge. The hospitality and suggestions of H. K. Moffatt during that period are gratefully appreciated.

Appendix A. Derivation of the pinch-off criterion

The four front matching conditions in (4.25) and (4.26) allow us to express the unknowns A, C, B_1 and κ_f in terms of three of the remaining five unknowns. Only the expression for κ_f is pertinent,

$$\kappa_f = \frac{(\alpha/\beta)[(1-\lambda_0^2\xi_0)(\gamma-1-D\gamma_2)/\xi_0-\gamma_1]}{D(1-\lambda_0^2)+(\alpha/\beta)^2\gamma\gamma_2}, \tag{A 1}$$

where $\lambda_0 = (\pi/2B)$ is the wavenumber of the surviving resonant term in the drop solution of (4.3) and (4.28) and the γ_i constants as functions of A_1 and c are given in (4.23). It is also easy to see from (4.23) that γ_2 is positive and γ_1 is larger than $(1-\lambda_0^2\xi_0)(\gamma-1)/\xi_0$ for $0<\beta<1/4$. Hence, D must be negative to ensure a positive κ_f.

On the other hand, the back matching conditions (4.12) and (4.13) yield an explicit expression for the curvature of the back matching locus for $(\alpha c)^{2/3} \gg \alpha$, which has been shown to be true,

$$\kappa_b = \left(\frac{2+\beta/2}{1+\beta}\right)^{1/2}. \tag{A 2}$$

https://doi.org/10.1017/S0022112096004879 Published online by Cambridge University Press

The back matching also allows us to eliminate x_b^0 and obtain the following two equations for the three remaining unknowns A_1, D and c:

$$\sin\omega + \omega\sin\epsilon = \xi_0\cos\epsilon\left(1 - \tfrac{3}{2}m\beta\right) - \sin\epsilon\left(\frac{3\pi}{2} - \epsilon - \frac{\hat{c} - A_1}{\alpha}\beta^{3/2}m^{1/2}\right), \tag{A 3}$$

$$\gamma = \frac{c\beta}{2+\beta}\left(A_1^{p_0} - \frac{1}{A_1^2}\right) + 1 - A_1^{p_0} = 1 + \frac{\cos\omega}{\sin\epsilon}, \tag{A 4}$$

where D has been replaced by ω through the formulae

$$D = -\left(\frac{\alpha}{\beta^{3/2}m^{1/2}}\right)\left(\frac{\sin\omega}{\sin\epsilon}\right), \tag{A 5}$$

$$\tan\epsilon = K(\beta)\frac{\alpha}{\beta^{1/2}}(\alpha c)^{-2/3}. \tag{A 6}$$

The parameters in (A 3) to (A 6) are $m = (1-\lambda_0^2)/\beta, K(\beta) = \xi_0[(3m^{1/2})/(2\hat{a})]^{3/2}$, and $\hat{a}$ and $\hat{c}$ are the Bretherton constants in (4.10). Because of their definitions in (A 4) to (A 6), ϵ and ω are bounded between 0 and $\pi/2$. Equation (A 4) can be rearranged into

$$c = \left(\frac{2+\beta}{\beta\sin\epsilon}\right)A_1^2\frac{(A_1^{p_0}\sin\epsilon + \cos\omega)}{(A_1^{p_0+2} - 1)} \tag{A 7}$$

and invoking the definition of $K(\beta)$, we get

$$(\alpha/\beta^{3/2})^{1/2} = c(\tan\epsilon)^{3/2}/K(\beta). \tag{A 8}$$

A convenient bound on ϵ can now be obtained. Since a positive κ_f is equivalent to a negative D and a positive ω from (A 1) and (A 5), (A 3) indicates that ω is positive only if ϵ is small and (A 3) also yields the condition

$$\tan\epsilon < \left(\frac{2\xi_0}{3\pi}\right)\left(1 - \tfrac{3}{2}m\beta\right) \leqslant \frac{2}{3\pi} \tag{A 9}$$

for $\beta\epsilon(0, 1/4)$.

We are now in position to impose a bound for positive κ_f. From (A 3) and the definitions of $K(\beta)$ and γ_i, it is clear that the denominator in (A 1) for κ_f is always positive. Consequently, κ_f is positive only if the numerator satisfies

$$(\gamma - 1 - D\gamma_2)(1 - \lambda^2\xi_0)/\xi_0 > \gamma_1. \tag{A 10}$$

Using the definitions of γ_1 and γ_2, (A 4) for γ and (A 5) and (A 7) for D and c, this inequality becomes

$$\begin{aligned}
&\frac{S\beta\cos\omega}{\xi_0} + \frac{S(2+\beta)^2\sin\omega}{\xi_0(1-\beta)K^2m^{1/2}\cos^3\epsilon}\left(\frac{A_1^{p_0}\sin\epsilon + \cos\omega}{A_1^{p_0+2} - 1}\right)^2 \\
&\quad\times A_1^3\left(3\cos\omega + \frac{2+\beta}{\beta}\left[\frac{A_1^{p_0}\sin\epsilon + \cos\omega}{A_1^{p_0+2} - 1}\right]\right) \\
&\quad> \frac{2(9+2\beta)}{(2+\beta)(1+\beta)}(A_1^{p_0}\sin\epsilon + \cos\omega) + p_0\frac{7+\beta}{1-\beta^2}A_1^{p_0}\ln A_1\left(\frac{A_1^2\cos\omega + \sin\epsilon}{A_1^{p_0+2} - 1}\right)
\end{aligned} \tag{A 11}$$

where $S = (1 - \lambda_0^2\xi_0)/\beta$ which is close to $(4/\pi) - 1 \sim 0.27$ for small β. The left-hand side of the above inequality is decreasing function of the amplitude A_1 at the front

https://doi.org/10.1017/S0022112096004879 Published online by Cambridge University Press

matching point while the right-hand side increases with increasing A_1. Because of the magnitude of S and $K^2(\sim 25)$, this inequality can hold only for amplitude A_1 values close to unity. We hence set $A_1 = 1 + \eta$ such that $\eta \ll 1$ and expanding (A 11) to leading order in η, we obtain the estimate

$$\eta < \left(\frac{Q(\beta)}{\beta}\right)^{1/3} \eta_*(\omega, \epsilon), \tag{A 12}$$

where $Q(\beta) = (S(1-\beta)^3)/(m^{1/2}K(\beta)(9+\beta)) \sim 10^{-3}$ for $\beta \in (0, 1/4)$ and

$$\eta_*(\omega, \epsilon) = (\sin\omega)^{1/3}(\cos\omega + \sin\epsilon)^{2/3}/\cos\epsilon. \tag{A 13}$$

It is easy to show that $\eta_*(\omega, \epsilon)$ has a maximum at $\cos\omega = \sqrt{2/3}$ for small ϵ which was established in (A 9). Consequently, a good estimate for the maximum value of η_* is $\eta_{max} = 2^{1/3}/\sqrt{3}$. A tight upper bound for (A 12) is then

$$\eta < \frac{2^{1/3}}{\sqrt{3}}(Q(\beta)/\beta)^{1/3}. \tag{A 14}$$

Since ϵ is small, $\sin\epsilon \sim \tan\epsilon \sim \epsilon$ and $\cos\epsilon \sim 1$ and an expansion of (A 3) and (A 4) allows explicit expressions for ϵ and η in terms of ω, α and β,

$$\epsilon \sim \frac{\xi_0(1 - 3m\beta/2) - \sin\omega}{(3\pi/2) + \omega - \beta^{3/2}m^{1/2}(\hat{c}-1)/\alpha}, \tag{A 15}$$

$$\eta \sim (\cos\omega + \epsilon)(1-\beta)K(\beta)(\epsilon/\alpha)^{1/2}\beta^{-1/4}. \tag{A 16}$$

Hence, both $\epsilon(\omega)$ and $\eta(\omega)$ are decreasing functions of ω and their maximum values lie at $\omega \to 0$. Equation (A 8) can also be expanded to yield

$$c \sim (\alpha/\beta^{3/2})^{1/2}K(\beta)\epsilon^{-3/2}. \tag{A 17}$$

Equations (A 16) and (A 17) now specify a family of solitary hump solutions parameterized by ω. The member with the minimum speed at $c(\omega \to 0)$ corresponds to one with a maximum amplitude of $1 + \eta(\omega \to 0)$ at the front matching line as seen from (4.22). This limiting member will have a concave front face and fall off if (A 14) is violated,

$$\eta(\omega \to 0) > \frac{2^{1/3}}{3^{1/2}}(Q(\beta)/\beta)^{1/3} \tag{A 18}$$

which, with (A 15) and (A 16), gives a critical condition in terms of α and β

$$\alpha < \beta^{1/6}L(\beta) + \frac{2(\hat{c}-1)}{3\pi}m^{1/2}\beta^{3/2}, \tag{A 19}$$

where $L(\beta)$ is given in (4.31) of the text. For $\beta \in (0, 1/4)$, the second term in (A 19) can be omitted and one obtains the simple expression (4.30) in the text.

REFERENCES

Aul, R. W. & Olbricht, W. L. 1990 Stability of a thin annular film in pressure-driven, low Reynolds-number flow through a capillary. *J. Fluid Mech.* **215**, 585–599.

Benjamin, T. B. 1957 Wave formation in laminar flow down an inclined plane. *J. Fluid Mech.* **2**, 554–574.

Bretherton, F. P. 1961 The motion of long bubbles in tubes. *J. Fluid Mech.* **10**, 166–188.

Chang, H. C. 1994. Wave evolution on a falling film. *Ann. Rev. Fluid Mech.* **26**, 103–136.

https://doi.org/10.1017/S0022112096004879 Published online by Cambridge University Press

Chang, H. C., Demekhin, E. A. & Kalaidin, E. N. 1995 Interaction dynamics of solitary waves on a falling film. *J. Fluid Mech.* **294**, 123–154.

Chen, Y. J. & Steen, P. H. 1996 Suppression of the capillary instability in the Rayleigh-Taylor slot problem. *Phys. Fluids* **8**, 97–102.

Cherhabili, A. & Ehrenstein, U. 1995 Spatially localized two-dimensional finite amplitude states in plane Couette flow. *Eur. J. Mech.* B/*Fluids*, **14**, 677–696.

Hammond, P. S. 1983 Nonlinear adjustment of a thin annular film of viscous fluid surrounding a thread of another within a circular cylindrical pipe. *J. Fluid Mech.* **137**, 363–384.

Huppert, H. E. 1982 Flow and instability of a viscous current down a slope. *Nature* **300**, 427–429.

Joo, S. W., Davis, S. H. & Bankoff, S. G. 1991*a* Long-wave instability of heated falling films: two-dimensional theory of uniform layer. *J. Fluid Mech.* **230**, 117–146.

Joo, S. W., Davis, S. H. & Bankoff, S. G. 1991*b* On falling film instabilities and wave breaking. *Phys. Fluids* A **3**, 231–235.

Kachanov, Y. S. 1994 Physical mechanism of laminar boundary layer transition. *Ann. Rev. Fluid Mech.* **26**, 411–483.

Kalliadasis, S., & Chang, H. C. 1994. Drop formation during coating of vertical fibres. *J. Fluid Mech.* **26**, 411–483.

Kerchman, V. I. & Frenkel, A. L. 1994 Interactions of coherent structures in a film flow: simulations of a highly nonlinear evolution equation. *Theor. Comput. Fluid Dyn.*, **6**, 235–254.

Manneville, P. 1990 Dissipative Structures and Weak Turbulence. Academic.

McCready, M. J., & Chang, H.-C. 1996 Formation of large disturbances on sheared and falling liquid films. *Chem. Engng Commun.* **142**, 347–359.

Oron, A. & Rosenau, P. 1989 Nonlinear evolution and breaking of interfacial Rayleigh-Taylor waves. *Phys. Fluids* A **1**, 1155–1165.

Pumir, A. Manneville, P. & Pomeau, Y. 1983 On solitary waves running down an inclined plane. *J. Fluid Mech.* **135**, 27–50.

Quere, D. 1990. Thin films flowing on vertical fibers. *Europhys. Lett.* **13**, 721–726.

Rosenau, P. Oron, A. & Hyman, J. M. 1992. Bounded and unbounded patterns of the Benney equation. *Phys. Fluids*, A **4**, 1102–1104.

Rothrock III, D. A. 1968 Study of flows down the underside of an inclined plane. PhD thesis, University of Cambridge.

Russo, M. J. & Steen, P. H. 1989 Shear stabilization of the capillary breakup of a cylindrical interface. *Phys. Fluids* A **1**, 1926–1937.

Van Hook, S. J., Schatz, M. F., McCormick, W. D., Swift, J. B. & Swinney, H. L. 1995 Long-wavelength instability in surface-tension-driven Benard Convection. *Phys. Rev. Lett.* **75**, 4397–4400.

Weiland, R. H. & Davis, S. H. 1981 Moving contact lines and rivulet instabilities. Part 2. Long waves on flat rivulets. *J. Fluid Mech.* **107**, 261–280.

Yih, C. S. 1963. Stability of liquid flow down an inclined plane. *Phys. Fluids* **6**, 321–334.

Young, G. W. & Davis, S. H. 1987 Rivulet instabilities. *J. Fluid Mech.* **176**, 1–31.

https://doi.org/10.1017/S0022112096004879 Published online by Cambridge University Press